Advanced Materials Technologies

ADVANCED MATERIALS TECHNOLOGIES
www.advmattechnol.com

RESEARCH ARTICLE OPEN ACCESS

Bidirectional Process Prediction in the Laser-Induced-Graphene Production Using Blackbox Deep Learning

Maxim Polomoshnov[1] | Nitheesh M. Nair[1] | Gerardo Hernández-Sosa[1,2,3,4] | Markus Reischl[1]

[1]Institute for Automation and Applied Informatics, Karlsruhe Institute of Technology, Eggenstein-Leopoldshafen, Germany | [2]Light Technology Institute, Karlsruhe Institute of Technology, Karlsruhe, Germany | [3]InnovationLab, Heidelberg, Germany | [4]Institute of Microstructure Technology, Karlsruhe Institute of Technology, Eggenstein-Leopoldshafen, Germany

Correspondence: Maxim Polomoshnov (maxim.polomoshnov@kit.edu)

Received: 26 December 2025 | **Revised:** 7 April 2026 | **Accepted:** 23 April 2026

Keywords: bidirectional prediction | blackbox modeling | deep learning | flexible electronics | machine learning | laser-induced graphene

ABSTRACT

Machine learning offers significant potential for automating manufacturing processes through prediction of parameters and properties. However, its adoption is limited by the needs for process-specific expertise, complex analytical models, and large, high-quality training datasets. This study introduces a streamlined, non-analytical blackbox deep-learning approach tailored to resource- and knowledge-limited settings. Applied to laser-induced graphene, an emerging technique for fabricating flexible electronics, this method uses a simple neural network for bidirectional predictions: forward estimation of graphene properties from laser parameters, and inverse prediction of laser settings from target properties. Using only a small dataset of 500 moderate-quality, high-variance samples, the model attained joint prediction accuracies of up to 95% on validation samples, and 96% in a functional flexible circuit. These results match or surpass more elaborate physics-informed or multi-component models in the literature, with minimal resources and no preprocessing. The method is widely applicable to various functional materials and fabrication techniques, minimizing dependence on prior knowledge, manual optimization, and specialized equipment. This demonstrates that high predictive performance can emerge from minimal overhead, making machine learning a practical, accessible instrument that democratizes intelligent manufacturing in graphene-based and related systems, enabling efficient and scalable real-world innovation.

1 | Introduction

In the field of organic and flexible electronics, laser-induced carbonization of organic polymers is fairly new. Among numerous microfabrication techniques, it is technologically analogous to non-impact printing processes, overperforming the latter in productivity, usability, robustness, and electrical properties of the output. It offers greater versatility and sustainability in comparison to printing due to its solvent-free nature, and due to the elimination of the post-processing steps, such as solvent evaporation and sintering. Therefore, a rapidly growing application of the method has been observable in such spheres as material science, energy, flexible electronics, sensors, advanced manufacturing, etc. [1–6]. For example, laser-patterned interdigitated electrodes on polyimide (PI) substrates, as illustrated in Figure 1a, serve effectively in flexible sensors and field-effect transistors. The process involves photothermal dissociation and graphitization of carbon-rich polymers (substrates) upon laser

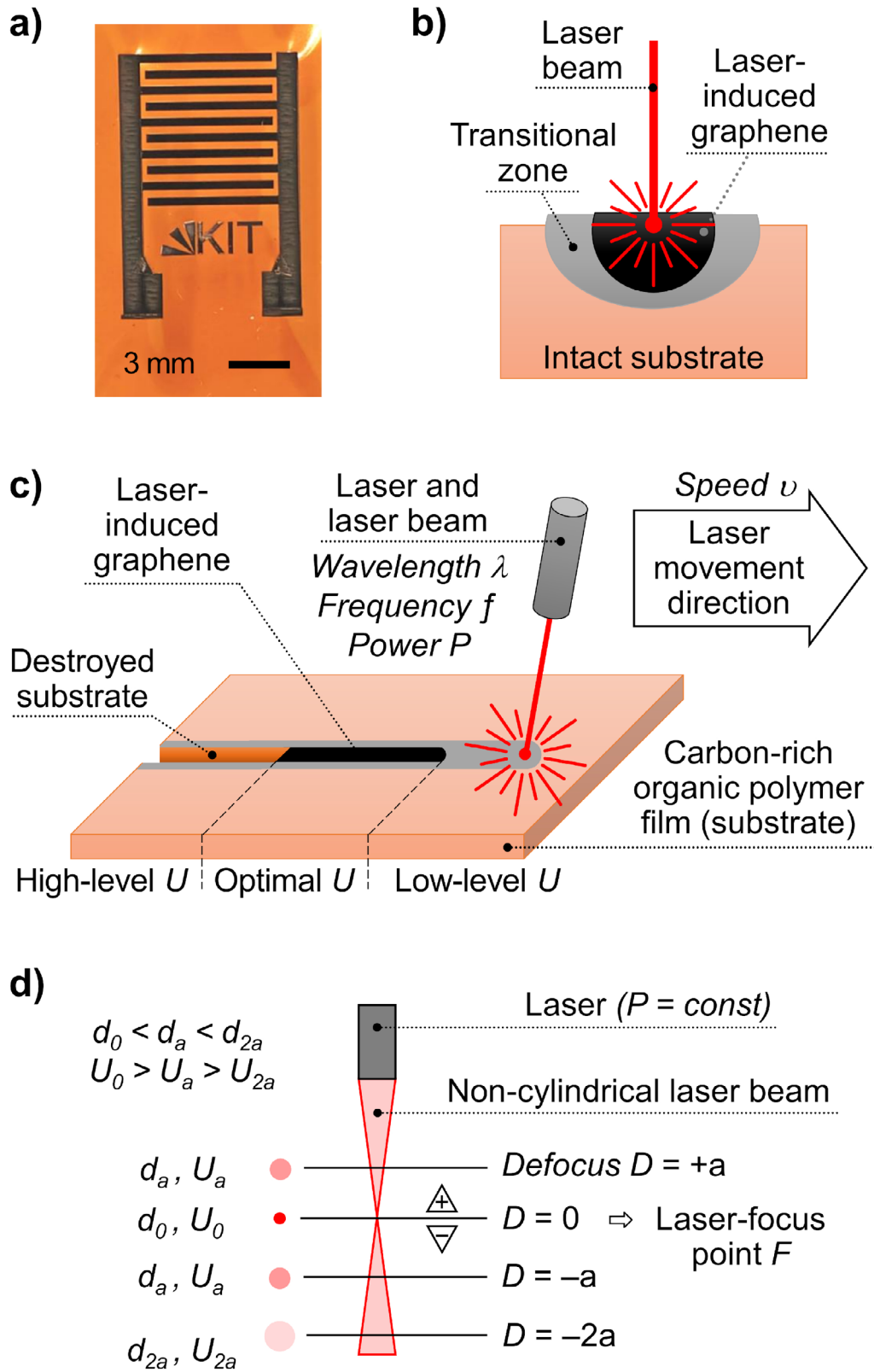

FIGURE 1 | Illustrations of laser-induced graphene (LIG) fabrication, related structures, and attributes. (a) Laser-patterned interdigitated electrodes on a polyimide substrate, suitable for applications in flexible sensors and field-effect transistors. (b, c) Schematics of LIG formation (combined and adapted from [1, 3, 5–7]). (b) Cross-section of a single line formed on a substrate film. (c) Manufacturing principle for a single line and its morphology depending on the applied energy density U. (d) Beam spot size d and energy density U as functions of the distance a between the substrate surface and the laser focal point F (adapted from [8]). The distance a defines the laser beam defocus D, which is positive when F is above the substrate surface and negative otherwise.

exposure, leading to the formation of laser-induced graphene (LIG) and a transitional zone where partial graphitization occurs, as depicted in Figure 1b,c.

Numerous laser parameters influence the outcome, with many interactions remaining only partially understood, which complicates manual process optimization. The morphology, properties, and structure of LIG depend primarily on the applied energy density (U), which in turn varies with laser wavelength, power (P), frequency, scanning speed (υ), and polymer interactions [1, 3], indicated in Figure 1b,c. A high-level U broadens LIG and transitional zones, but risks pyrolysis, whereas a low-level U narrows the zones, but potentially yields insufficient graphitization (Figure 1c). Precise adjustment of laser beam parameters (LBP) achieves optimal U values. This study identifies three primary U regimes: optimal (i.e., mid-level) for stable, conductive LIG with high yield; high-level, resulting in over-graphitization, pyrolysis decomposition, or substrate destruction [1, 9, 10]; and low-level, preventing reliable conductive LIG formation, though partial graphitization or thermal damage may occur [1, 3]. Energy delivery also depends on beam geometry. As shown schematically in Figure 1d, beam diameter (d) varies along its propagation, reaching a minimum at the focal point (F). Defocus (D) denotes the distance between F and the substrate surface—positive when F lies above the surface and negative otherwise. Greater $|D|$ dissipates energy, reducing U while increasing overlap of adjacent scan spots due to beam expansion, which causes multiple exposures [1, 5, 8, 11]. Thus, D ranks among the critical LBP in LIG fabrication.

Despite its apparent simplicity, LIG patterning requires careful consideration of multiple laser parameters and material characteristics to achieve targeted geometrical and functional properties (PP) [4, 7, 11, 12]. Reliable, reproducible fabrication of conductive LIG films remains challenging, as precise manual LBP optimization proves labor-intensive, often leading to excess material consumption and resource waste. Machine learning (ML) models offer advantages over manual methods by enabling efficient data collection, processing, and correlation, thereby enhancing process efficiency and sustainability [4, 7, 13]. Deep learning (DL), a subset of ML, employs numerical approaches to emulate neural operations, with multilayer perceptrons (MLPs) serving as fundamental neural-network (NN) architectures [14]. Blackbox DL treats internal processing as opaque, allowing a streamlined strategy that avoids the requirements for process-specific knowledge or complex submodels [15–17]. This approach suits resource-constrained settings lacking advanced equipment, large datasets, or specialized expertise. Further details on its principles appear in Note S1 and Figure S1 [7, 14–24].

In the field of LIG, the application of ML to predict a fabrication process was considered in numerous state-of-the-art publications. Xie et al. [11] employed the Bayesian-optimized Gaussian Process Regression to predict functional properties of fluoride-doped LIG from LBP. Namely, hydrophobicity and electrical resistance of the fabricated LIG surface were assessed simultaneously. Ghimire et al. [4] introduced Bayesian optimization of process parameters, focusing on minimizing sheet resistance, and on maximizing fabrication yield in LIG-based glucose sensors. Santos-Ceballos et al. [13] simulated the LIG-fabrication process, using a digital-twin NN-based model. Xia et al. [23] first applied a twofold deep-transfer-learning model to classify LIG in a vision-based process monitoring. Chen et al. [25] developed a lazy ML algorithm to correlate LBP and the LIG morphology and resistance. Le et al. [12] predicted sheet resistance of LIG with respect to the applied laser energy. Their model framework combined two algorithms assessing multiple laser parameters. Murray et al. [26] proposed an analytical Design-of-Experiment strategy to optimize LBP in LIG fabrication, to bypass the need for an extensive training dataset in complex ML models.

Beyond LIG, the ML-assisted prediction of the properties from process settings was reported for such related branches, as graphene fabrication, flash Joule heating, and functional printing. Sattari et al. [24] and Beckham et al. [27] predicted the graphene yield with a physics-based ML framework, and with an eXtreme Gradient Boosting (XGB) regression model, correspondingly. Jin et al. [28] explored the application of a cycled long short-term memory model to predict mechanical properties and performance of nickel-graphene nanocomposites, based on the input molecular-dynamics data. Kim et al. [29] designed an ML approach to optimize jetting-control signal in the inkjet process, with respect to the ink properties. Huang et al. [30] designed a physics-based DL framework to predict droplet appearance from the jetting-control signal and ink properties. Zhao et al. [31] described a double-direction physics-informed MLP model for an application in the *laser powder bed fusion* printing process. They compared efficiency of the model on sole physically-fabricated samples, and on a hybrid dataset with mechanistic modeling data.

The literature survey revealed the following gaps.

1. Most studies employed interpretable physics-informed or complex multi-component ML/DL frameworks for property prediction and classification [7, 11–13, 23, 24, 28–31]. The requirement for large training datasets exceeding several thousand samples hindered broader adoption of deep learning despite its demonstrated potential.
2. With rare exceptions, investigations focused only on forward prediction of outcome properties from process parameters, but not vice versa [11–13, 24, 25, 27–29]. Yet, determining the laser settings necessary to achieve specific product characteristics holds greater practical relevance for manufacturing.
3. Many researchers also restricted analysis to predefined parameter ranges and excluded precarious data [7, 12, 13, 19, 25, 31]. That limited the number of considered variables, reduced real-world robustness, and demanded extensive preliminary analysis and high-quality data preparation, thereby elevating labor costs.
4. Precise morphological assessment of LIG typically relied on Raman spectroscopy [1, 3, 4, 7, 13, 24]. This is a standard yet equipment-intensive technique requiring costly instrumentation and substantial manual effort. Faster, naïve evaluation methods better suited to industrial scaling received little attention at the laboratory level.

To address the limitations, we reposition the MLP as an innovative streamlined and non-analytical blackbox strategy, optimized for industrial scalability in LIG production. Unlike complex, resource-intensive frameworks, such as digital-twin models [13],

TABLE 1 | Laser-beam properties for fabrication of training lines (Dataset A).

Laser-beam parameters	Values applied
Laser power P [W]	4, 6, 8, 10, 12
Laser movement speed across the substrate υ [mm/s]	25, 50, 75, 100, 125, 150, 200, 250
Laser-beam defocus D [mm]	−0.3, 0, 0.3, 0.5

multi-NN architectures [23], or physics-informed ML approaches [24], the proposed method requires minimal prior knowledge, no data filtering, and small datasets. Therefore, it suits environments with constrained computational resources, time, or expertise.

This work assesses the feasibility of a blackbox DL approach for bidirectional prediction in LIG fabrication—enabling both estimation of LIG properties from given laser parameters and, conversely, determination of the required parameters to achieve targeted properties. A simple MLP served as the core blackbox data transformer. Model training and accuracy evaluation relied on a modest set of fabricated LIG structures. Subsequently, the trained model predicted laser parameters for electrodes in a functional flexible electronic circuit (demonstrator) and verified results within the same stage. The attained model performance was benchmarked against conventional regression and literature methods, focusing on dataset size, data filtering practices, model complexity, and prediction directionality. The overall workflow culminated in the successful fabrication and validation of a set of demonstrators.

2 | Results and Discussion

2.1 | Collected Samples

The primary training dataset (Dataset A [32], Figure S2) consisted of 500 LIG lines, organized into 100 groups of five identical lines, each fabricated using the same laser parameters, listed in Table 1. Microscopic inspection revealed a range of LIG morphologies that depended on the applied energy density U, as shown in Figure 2a–e. Low energy densities produced either no visible lines (Figure 2a) or partially carbonized, non-conductive structures (Figure 2b). Optimal conditions yielded functional lines with a conductive graphene core (dark central region) surrounded by a gray boundary zone (Figure 2c). High energy densities caused pyrolysis decomposition, resulting in non-conductive lines with vertical surface cracks (Figure 2d) or complete destruction of the graphene core (Figure 2e). The entire process: preparation, laser-patterning, sample characterization, and data collection required approx. three hours.

Two additional datasets served for validation. Dataset B [32] included 100 validation lines arranged in 20 groups of five lines. The groups were evenly split between direct and inverse prediction tasks. LBP and target LIG properties were randomly selected within predefined ranges, listed in Table S1. Dataset B is represented in Figure 2f and Figure S3. Dataset C [32] extended validation to more complex geometries, featuring 13 rectangular shapes: seven for direct prediction, six for inverse prediction (Figure 2g,h; Figure S4).

2.2 | Analysis of Collected Data

The systematically collected datasets, encompassing controlled training samples and diverse validation structures, formed the basis for initial data-quality assessment. These data enabled development of a predictive model, and enabled subsequent evaluation of its prediction accuracy on actual samples.

For all fabricated samples, the actual R, W, and Q values were measured. For validation rectangles in Dataset C, the equivalent resistance R_{eq} was calculated because overlapping prevented direct measurement of R and W for individual lines. These measured values correlated with the applied lasing parameters LBP, and, hence, with the energy density U. In accordance with the blackbox approach, the data underwent treatment "as is", without incorporating prior knowledge of quality [15–21]. Potential LIG detachment received no consideration, which increased overall variance, but enhanced model generalizability. Figure 3 summarizes the collected data and key results from this work, with discussion provided below.

Analysis of Dataset A (training lines) identified substantial variance in both R and W values, as shown in Figure 4a and Figure S5, with corresponding accuracy metrics listed in Table S2. The unbiased relative standard deviation exceeded the critical value $\%RSD^{*}_{crit}$ for both properties ($1.76 \gg 0.33$ for R; $0.53 > 0.33$ for W). That indicated a need for data improvement through refabrication or filtering of low-quality entries [33–35]. At $U \lesssim 15$ J/mm^3, the applied energy was too low to form conductive LIG. As U increased, line width W and resistance R expanded (Figure S5a), while minor declining trends emerged for quality Q and the joint accuracy metric J (Figure S5b), caused by an increased production of fragile LIG at higher U. Over-graphitization occurred near $U \approx 115$ J/mm^3, with a complete substrate destruction at greater values. The identified conductive range (approximately 15–115 J/mm^3) guided fabrication of validation samples.

Distribution plots in Figure 4b,c and Figure S5c,d confirmed the high variance in training data for R (Figure 4b), W (Figure 4c), Q (Figure S5c), and J (Figure S5d), with related metrics listed in Table S2. PCC indicated weak to moderate relationships between trend and actual values, while R^2 scores demonstrated poor trend fitting due to variance. The discrete variable Q exhibited stronger correlation and fitting. The resulting J value reached 75.6% ± 35.8% ($R^2 = 0.04$; PCC = 0.20), corroborated by regression analysis at 45.4% ± 32.4%. Albeit potential model inaccuracy, inclusion of such high-variance data preserved real-world applicability, as the model's error bounds accounted for inherent process uncertainties and supported safer scaling to production.

Despite the limited size and high variance of training data, validation samples in Datasets B and C yielded decent prediction accuracy. The selected U range (20.9–97.8 J/mm^3) aligned fully with the conductive zone, as in Figure 4a and Figure S5a,b. Fifteen lines and two rectangles at $U \gtrapprox 100$ J/mm^3 received correct "non-conductive" predictions from the NN. Correlation plots for R, R_{eq}, W, Q, and J appear in Figures S6c–f and S7c–e,

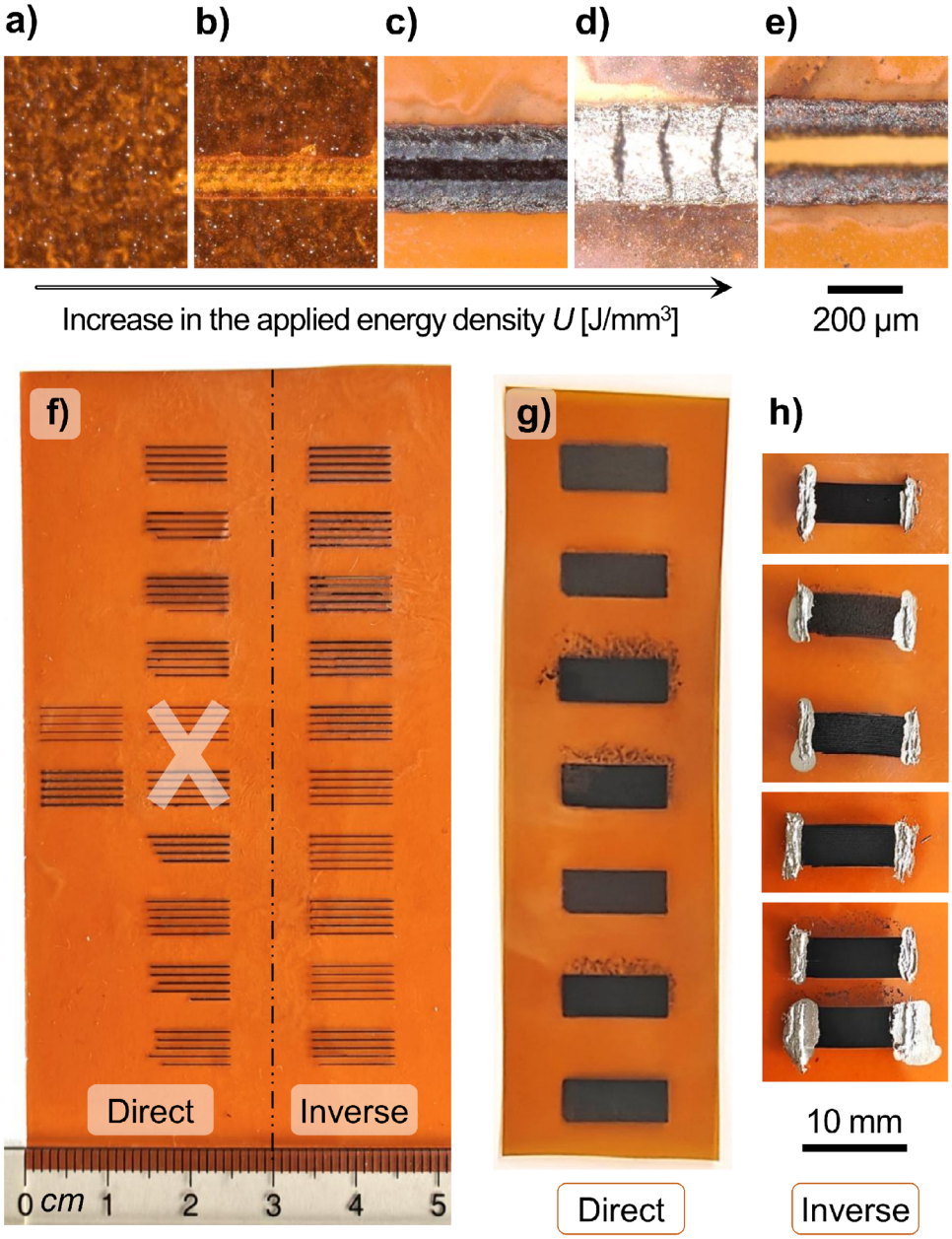

FIGURE 2 | Microscopic and photographic images of laser-induced graphene samples across datasets, illustrating morphology variations and validation outcomes. (a–e) Representative cropped microscopic images (same scale) of laser-patterned lines from Dataset A. (a) No visible line formed due to very low density U of the applied laser energy. (b) Visible, but non-functional, partially carbonized line resulting from low U to induce conductive graphene. (c) Functional line with a distinct conductive graphene core (central black region) surrounded by a gray transitional zone. (d) Non-conductive line exhibiting vertical surface cracks caused by high U leading to pyrolysis decomposition. (e) Completely destroyed graphene core with a remaining gray transitional zone due to very high U. (f–h) Cropped digital photographs of validation samples. (f) Validation lines from Dataset B ($n = 100$), divided into groups for direct prediction (randomly generated laser beam parameters to predict resistance R, width W, and quality Q) and inverse prediction (randomly generated R, W, and Q to predict power P, speed υ, and defocus D); samples marked with X indicate incorrectly set parameters and were excluded. (g, h) Validation rectangles from Dataset C ($n = 13$, same scale): (g) immediately after lasing, and (h) after manual application of conductive varnish to ensure uniform connection of all individual lines.

with metrics in Tables S3 and S4. Both validation sample types showed moderate to very strong correlations (R^2 and PCC) between predicted and ground-truth values, with no notable differences between direct and inverse workflows. Joint accuracy J attained 80.8% ± 9.4% for lines (Dataset B; $R^2 = 0.74$; PCC = 0.86) and 91.8% ± 7.8% for rectangles (Dataset C; $R^2 = 0.93$; PCC = 0.96). Corresponding regression values were considerably lower (62.7% ± 31.9% and 63.2% ± 32.7%). Thus, the developed model delivered statistically significant prediction accuracy. That confirmed the viability of the approach and enabled practical benefits, such as reduced material waste through targeted optimization.

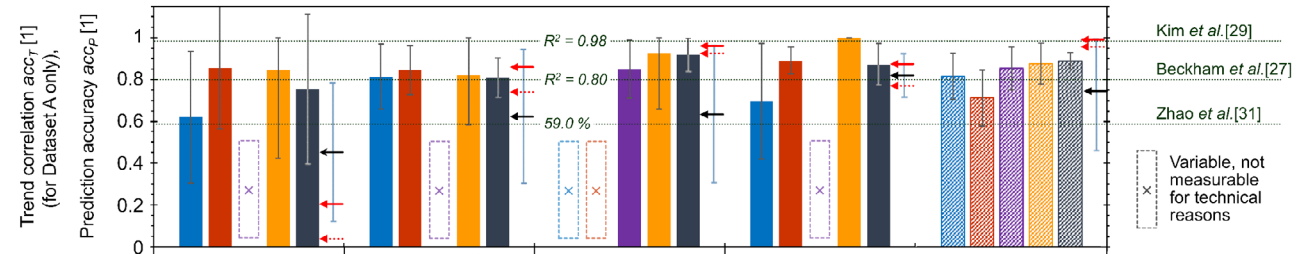

Product properties	A: Training lines	B: Validation lines	C: Validation rectangles	D: Twofold control		Laser-beam parameters
	n = 500	n = 100	n = 10	Run B, n = 22	Run A, n = 18	
Resistance R	61.90 ± 31.58	81.33 ± 15.40	—	69.60 ± 19.12	81.51 ± 10.85	Power P
Line width W	85.72 ± 29.18	84.38 ± 11.74	—	89.12 ± 6.53	71.00 ± 13.26	Movement speed v
Equivalent resistance R_{eq}	—	—	84.92 ± 13.72	—	85.33 ± 10.28	Defocus D
Line quality Q	84.29 ± 41.87	82.00 ± 23.58	92.31 ± 26.65 (n = 13)	100.0 ± 0.0	87.35 ± 9.69	Energy density U
Joint accuracy J	75.57 ± 35.83	80.79 ± 9.43	91.82 ± 7.84	87.28 ± 9.98	88.83 ± 3.92	Joint accuracy J
Regression	45.36 ± 32.43	62.70 ± 31.88	63.20 ± 32.73	82.07 ± 10.45	74.77 ± 28.59	Regression
R^2 score	0.040	0.743	0.926	0.769	0.964	R^2 score
PCC score	0.200	0.862	0.962	0.877	0.982	PCC score

FIGURE 3 | Overview of the collected data and key results from the present study on laser-induced graphene fabrication. For comparison, edge cases of prediction accuracy reported in the literature are indicated for illustrative purposes. The coefficient of determination R^2, Pearson correlation coefficient (PCC), and regression analysis are provided for the joint value J only, as it represents the collective central tendency across the multiple variables considered. Error bars denote standard deviation.

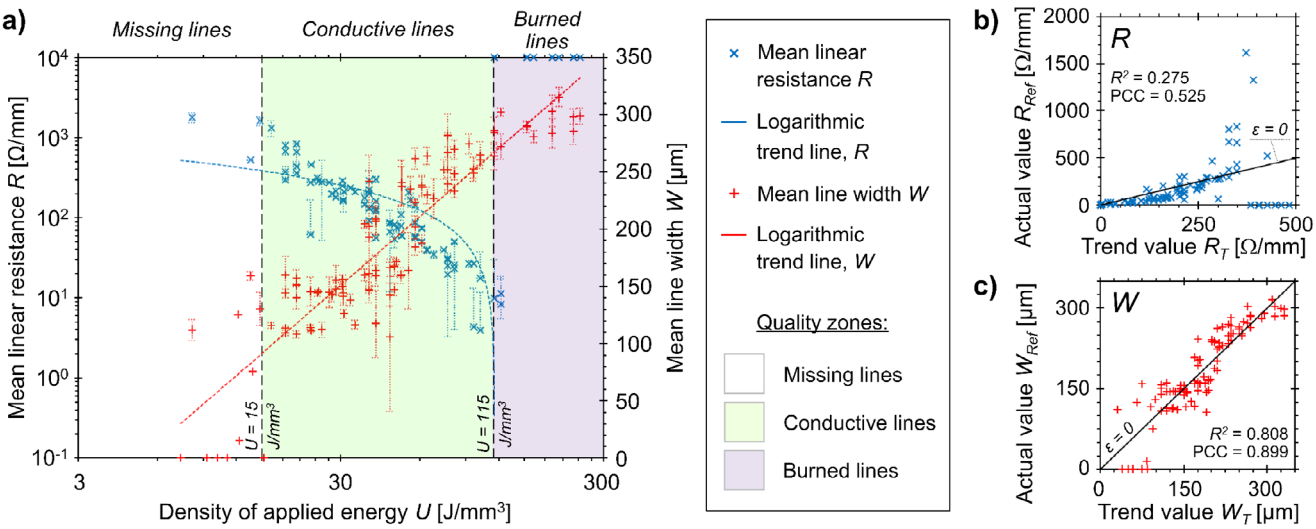

FIGURE 4 | Analysis of training data from Dataset A. (a) Mean values of linear resistance R and line width W, as functions of applied energy density U, shown with logarithmic trend lines. Three distinct quality zones are identified based on the appearance of fabricated laser-induced graphene samples. (b, c) Distribution plots comparing actual mean values against mathematically expected trend values (derived from the trend lines in (a) for (b) R and (c) W. The diagonal line $\varepsilon = 0$ indicates perfect agreement. Corresponding coefficients of determination R^2 and Pearson correlation coefficients (PCC) are provided. Error bars in (a) represent standard deviation.

2.3 | Twofold Control of Data Handling

In two runs of the twofold-control workflow, restoration capabilities of synthetic data were assessed. The corresponding Dataset D [32] consisted of 150 randomly generated combinations of LBP and LIG properties PP. In run A, the model restored 25 LBP combinations from given PP values, yielding metrics detailed in Table S5. The mean joint accuracy J reached 86.8% ± 5.0% (R^2 = 0.92; PCC = 0.96). Two key observations emerged. First, prediction accuracy proved higher for LBP associated with conductive lines, compared to values outside this range (88.8% ± 3.9% versus 81.6% ± 3.4%, respectively; Figure S8a). Second, although scatter plots revealed weak correlation between initial and restored individual laser settings P and D (Figure S9b,d; R^2 ≈ 0.03; PCC = 0.16–0.19), the restored U and J values closely matched the originals (Figure S9e,f; R^2 > 0.70; PCC > 0.83). The NN appeared to refine suboptimal process parameters to achieve intermediate predicted LIG properties while preserving applied laser energy U and target PP. This is crucial for proactive, AI-supported manufacturing lines, determining an ideal initial parameter set for production startup. A conventional regression model achieved lower accuracy of 74.8% ± 28.6%.

In run B, the model processed 25 PP combinations from given LBP values, with metrics reported in Table S6. The mean J value was 84.7% ± 11.9% (R^2 = 0.66; PCC = 0.81), influenced notably by the high variance in R (Figures S8b and S9g–h). stinction between conductive and non-conductive lines became more pronounced than in run A. For conductive lines with U < 115 J/mm^3, correlations ranged from moderate to very strong (Figure S9g,i,k,m), producing J = 87.3% ± 10.0% (R^2 = 0.77; PCC = 0.88), compared to 82.1% ± 10.5% for regression. In contrast, for U > 115 J/mm^3, J was 66.1% ± 8.0% (Figure S9h,j,l,n). As reported in [44], such small correlations are typical for nonfunctional samples fabricated with suboptimal settings. Thereby, even sparse data from such regimes provide sufficient foundation for model training. Future improvements for high U should prioritize optimization of the quality property Q to ensure appropriate energy application. One approach involves partitioning a single line into multiple parallel ones to create rectangular structures [36], thereby adjusting R, W, and U accordingly. Such enhancements lay beyond the scope of this study, but warrant investigation in subsequent work.

Overall, the NN-based twofold control explicitly accounts for the common one-to-many relationship between fabrication parameters and product properties. In LIG manufacturing, multiple LBP combinations can produce nearly identical functional, dimensional, and quality outcomes owing to the underlying nonlinear process physics. Accordingly, the inverse NN is intended to identify a practically useful LBP combination that achieves the desired LIG properties. Instead of a mere restoration of the input parameter set, it is designed to verify attainability of such properties. Furthermore, the inverse NN is anticipated to provide an optimized LBP combination that reliably reproduces the target PP within acceptable tolerances. Thus, the data-restoration accuracy on Dataset D exhibited optimization performance comparable to that obtained on validation samples (Datasets B and C). This capability highlights potential applications in inspecting and optimizing process parameters as well as designing LIG-based circuitry. The practical implications of these findings became evident in the flexible demonstrator.

2.4 | Flexible Demonstrator

To showcase the model's effectiveness in real-world applications, we applied the trained model to predict laser parameters for targeted LIG properties of a flexible circuitry. Photographs of the finalized demonstrator are shown in Figure 5a. Target properties for the LIG electrodes ($W^*_{LIG} \approx 250$ µm, $R^*_{LIG} \approx 40$ Ω/mm, $Q_{LIG} = 1$) were established beforehand, as detailed in Note S2 [37–39]. Using the inverse prediction workflow (run B in the twofold-control process), the model generated a single set of LBP (p = 9.2 W, υ = 61.1 mm/s, D = 0 mm) required to achieve these properties. The corresponding energy density U fell well within the conductive-line range, eliminating the need for further design optimization. Synthetic control properties (R_s, W_s, Q_s) derived from these LBP values were then evaluated against the targets. Subsequently, 10 identical LIG electrodes were fabricated using the predicted parameters, and their actual properties (R_a, W_a, Q_a) were measured (Dataset E [32]).

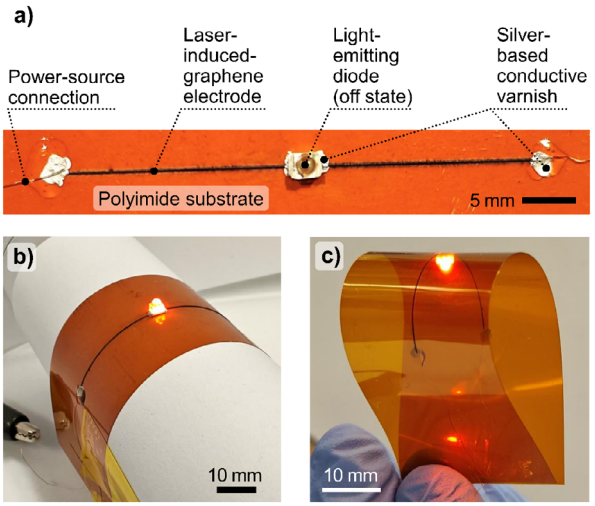

FIGURE 5 | Photographs of the fabricated flexible LED circuit using machine learning-predicted laser parameters, demonstrating operational functionality. (a) Flat demonstrator in the "off" state. (b, c) Variously curved demonstrator in the "on" state.

Comparison revealed high prediction accuracy, with joint accuracy J_s = 94.6% for the synthetic properties and J_a = 95.9% ± 1.5% for the measured ones. Table 2 presents the prediction and evaluation results across operational stages. The fabricated electrodes exhibited a measured linear resistance of 39.7 Ω/mm ± 2.3 Ω/mm, closely aligning with the target. The completed circuit operated stably at 5 V, powering the LED without degradation over 100 cycles and demonstrating mechanical flexibility under bending, as illustrated in Figure 5b,c. These outcomes confirm the model's value for rapid process optimization in flexible electronics. The successful demonstration underscores the advantages of the proposed approach when compared to methods reported in the literature.

2.5 | Comparison to Literature

Prior research on ML applications in LIG and related fabrication processes has focused on sophisticated models that prioritize interpretability and precision, often at the cost of practicality. A multitude of evaluation metrics across studies complicates direct comparisons, particularly for a non-academic audience. Reported accuracies vary from 80.0% to 96.6% for regression-based tasks, and from 95.4% to 98.0% for classification tasks. The lower 59.0% accuracy in [31] differs notably, as researchers attained it with solely physically manufactured data without supplementary modeling—similar to the raw, unenhanced strategy in the present work. Bidirectional workflows capable of predicting between process parameters and product properties in both directions appear only in that same investigation [31].

Most studies adopted white- or graybox methodologies, with six using standard ML techniques [11–13, 24, 25, 27] and five utilizing more complex DL models [23, 28–31], two of which integrated image transformation [23, 30]. Physics-informed or digital-twin frameworks, including physics-informed NNs, featured in six works [13, 23, 24, 29–31]. They typically

TABLE 2 | Demonstrator prediction and evaluation: Operational stages, related variables, and their values.

①	②	③	④	⑤	⑥
Target properties	**Laser-beam parameters, predicted from ① (n = 1)**	**Control synthetic properties, predicted from ② (n = 1)**	**Prediction accuracy [1], from ① and ③ (n = 1)**	**Actual properties, measured upon fabrication via parameters from ② (n = 10)**	**Prediction accuracy [1], from ① and ⑤ (n = 10)**
$R^*_{LIG} = 40.0\ \Omega/\text{mm}$	$P = 9.22$ W	$R_s = 35.8\ \Omega/\text{mm}$	0.895	$R_a = (39.7 \pm 2.3)\ \Omega/\text{mm}$	0.948 ± 0.019
$W^*_{LIG} = 246.9\ \mu\text{m}$	$v = 61.11$ mm/s	$W_s = 261.0\ \mu\text{m}$	0.946	$W_a = (230.1 \pm 7.6)\ \mu\text{m}$	0.932 ± 0.031
Q_{LIG} = "1"	$D = 0.0$ mm	Q_s = "1"	1.0	Q_a = "1"	1.0 ± 0.0
Joint values	$U = 76.84\ \text{J/mm}^3$	$J_s = 0.946$		$J_a = 0.959 \pm 0.015$	

TABLE 3 | Comparison of key attributes of our and reported ML models.

Aspect	Present work	Reported works [11–13, 23–25, 27–31]
Model type	Blackbox MLP	Various: physics-informed and complex ML
Dataset size [samples]	500 unfiltered moderate-quality (*%RSD** > 0.33)	≫10,000 unfiltered moderate-quality (*%RSD** > 0.33), or 103–648 filtered high-quality (*%RSD** < 0.33)
Data preprocessing	None: data are ready to use 'as is' immediately after collection	Filtering, augmentation, or physics constraints require up to several days after initial data collection
Model complexity	Single MLP, non-physics-informed, and non-analytical model	Multi-NN, physics-informed NN, digital-twin, or hybrid analytical models
Bidirectional capability	Yes	Only unidirectional, except for [31]
Prior knowledge required	None: usage of conventional data, no complex data processing or modeling, no sophisticated ML model preparation or integration	Extensive: special expertise in the data collection, data processing, physics-informed data modeling, ML model preparation, and implementation
Resource intensive	No: model training on an average PC is feasible; several hours are required for data collection, model preparation, and model training	Yes: training of complex models requires an increased computing power; preparation and training of complex models, and physics-informed data modeling require several days to weeks.
Accuracy [1]	$R^2 = 0.74$–0.96 PCC = 0.86-0.98	0.80–0.98, depending on data quality; 0.59 for a comparable approach in [31]

involved prior data modeling, enhancement, or filtering to boost performance, except in [31]. Although such preprocessing improved apparent predictive capabilities, it substantially increased labor and complexity. Studies that relied on raw data instead required large datasets of up to 883 000 samples [27–30], demanding considerable resources for acquisition and management.

In contrast, the present study employed a lightweight blackbox DL model based on an MLP, eliminating preliminary physics-based analysis or data refinement. Compared to prior studies, our blackbox MLP approach distinguished itself through simplicity and efficiency in LIG prediction. Table 3 compares its key attributes with representative physics-informed or complex ML/DL models. With an untreated dataset of 500 high-variance samples, the approach achieved prediction accuracies up to 95%. Alongside, R^2 and PCC values ranging from 0.74 to 0.98 indicated strong to very strong agreement between predicted and measured results. These outcomes match or exceed those from more elaborate ML methods in the literature, while the present technique requires far less specialized equipment, domain expertise, and preparatory effort. For instance, a comparable approach reported in [31] demonstrated accuracy of 0.59 on a physical yet smaller untreated dataset. Detailed attributes of the NN from prior works appear in Note S3 and Table S7, with extreme comparisons illustrated in Figure 3.

3 | Conclusion and Future Work

This study presents a novel adaptation of blackbox deep learning as a streamlined, non-analytical approach for bidirectional

prediction in LIG fabrication. Utilizing a simple multilayer perceptron trained on a modest dataset of 500 raw samples, it bypasses incorporating domain-specific knowledge. Achieving joint accuracies of up to 95% on validation samples and 96% for flexible circuitry, the proposed method serves as a practical alternative to resource-intensive whitebox frameworks that rely on physics-based or deterministic submodels for enhanced explainability. While such sophisticated approaches are ideal for highly complex, safety-critical processes, the narrower complexity of LIG fabrication favors simplified, but cost-effective blackbox models. By enabling optimization of process parameters to attain desired product properties, this integration of machine learning accelerates automated data processing, reducing optimization costs and material waste.

Unlike prior studies, which often demanded large datasets, extensive preprocessing, or focused solely on forward prediction, this work demonstrates bidirectional capability on high-variance data. This first purely blackbox deep learning application in LIG manufacturing does not require analytical models or specialized equipment, and mirrors real industrial constraints. Validation on linear and rectangular shapes confirms scalability and effective management of energy-dependent morphological variability and substrate fragility. This methodology lowers barriers to machine learning adoption in small laboratories and high-throughput settings, shortening development timelines and broadening LIG applications in flexible electronics, surface engineering, and energy systems. Future improvements may involve explicit overlap parameterization, advanced characterization, and model-hyperparameter optimization to address limitations from data degradation and fabrication inconsistencies. The framework's versatility extends to diverse fields, including industrial production, microfabrication, metallurgy, power generation, agriculture, and healthcare, by enabling rapid process-output correlations without time-intensive analytical models and unnecessary waste generation.

4 | Methodology

4.1 | Workflows and Datasets

To accomplish the objectives of the study, several interconnected steps guided the bidirectional prediction approach in LIG fabrication.

1. Correlated input and output variables were identified and quantified to establish a foundation for modeling.
2. A NN was designed and configured for both direct and inverse predictions, establishing the system to handle forward and backward mapping.
3. Output data were generated through NN predictions from the input dataset, simulating potential outcomes.
4. A series of LIG samples was produced using the NN-derived parameters to test real-world applicability.
5. The NN-predicted values were compared against physically measured variables, evaluating prediction accuracy, and accounting for data variance to assess overall reliability.

LBP and PP served as interchangeable input and output data for these predictions. Specifically, they included:

a. LBP: laser-beam power P [W], movement speed υ [mm/s], and defocus D [mm]; and
b. PP: linear electrical resistance R [Ω/mm] as a functional attribute, dimensional width W [µm] as a geometric characteristic, and conductivity-specific quality Q {"0", "1"} as a binary indicator of the LIG's overall suitability. Thus, R represented functional, W dimensional, and Q quality properties of the lines.

In this framework, shown in Figure 6, the direct workflow ("signal to properties") used LBP inputs to estimate PP outputs, while the inverse workflow ("properties to signal") reversed this by deriving LBP from desired PP. These processes facilitated efficient parameter optimization without extensive manual adjustments, addressing the challenges of complex process setups in resource-limited settings. The prediction direction depended on the dataset combination, as shown in Figure 6a,b. Both processes required physical sample fabrication using provided or predicted LBP.

Only LIG properties PP were directly measurable, which shaped the workflow design. Ultimate NN prediction accuracy arose from comparing NN-predicted PP (in direct prediction, Figure 6a), or required PP (in inverse prediction, Figure 6b) against measured (ground-truth [40]) values. Use of the same NN across both workflows facilitated bidirectional parameter adjustment. Training data, collected from fabricated and characterized samples, included known LBP and associated PP. Therefore, the data were equally suitable for both direct and inverse predictions—i.e., bidirectional. Validation of NN-predicted values employed a twofold-control workflow, indicated in Figure 6c. During that synthetic reconstruction, the two separately pre-trained NNs on identical bidirectional training data performed double conversion of random inputs. Run A examined LBP → PP → LBP conversion; run B focused on PP → LBP → PP. Unlike physically produced validation samples, inputs and outputs in these runs allowed direct comparison. This dual method resembles the CycleGAN architecture applied in generative ML [41–43].

Datasets supporting these workflows included Dataset A [32] for initial model training, Dataset B [32] for model validation on simple linear structures, and Dataset C [32] for model validation on more complex rectangular structures required for a transition from simplistic samples to elaborated patterns. Parameter and property ranges for both types of validation samples are indicated in Table S1, with random generation within specified limits to ensure broad coverage. In addition, Dataset D [32] enabled model validation using a twofold synthetic reconstruction of input variables.

4.2 | Sample Design

The physical samples comprised linear and rectangular LIG structures on polyimide substrates, designed to generate a range of quality levels for thorough model testing and validation, as depicted in Figure 7. Each line measured 10 mm in length with a one mm axial spacing. A group of five parallel lines to be

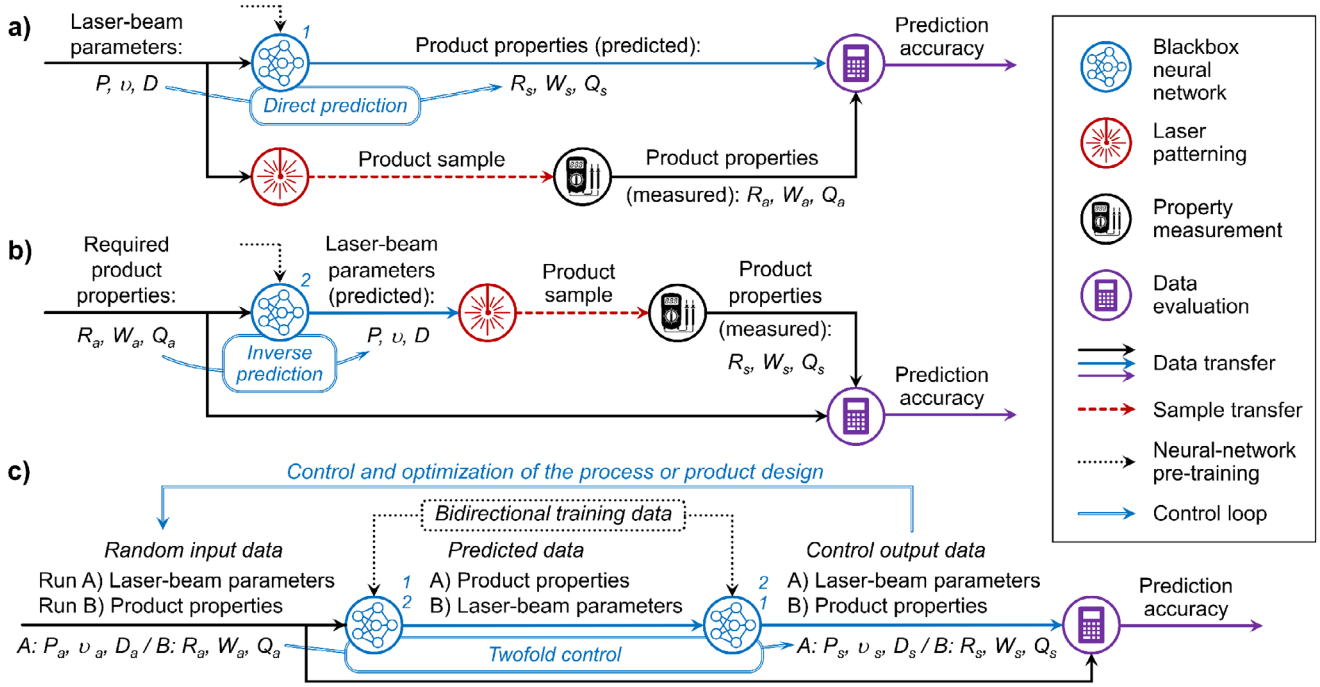

FIGURE 6 | Schematics illustrating the neural network-based prediction workflows and accuracy evaluation for laser-induced graphene (LIG) fabrication. (a) Direct-prediction workflow, in which laser beam parameters (LBP) serve as inputs to predict process properties (PP). (b) Inverse-prediction workflow, in which desired PP are used as inputs to estimate the required LBP. (c) Twofold-control workflow for evaluating prediction accuracy through synthetic reconstruction, where two separately pre-trained neural networks operate sequentially on identical bidirectional training data without physical sample fabrication. In (c), index "a" denotes actual input data, and index "s" denotes synthetic output data.

fabricated under identical laser parameters built a set, depicted in the generic digital layout in Figure 7a. These groups formed a matrix on the substrate, organized by varying laser settings, as in Figure 7b. Thus, the outcomes were expected to span from unformed structures under low energy to damaged ones under high energy [1, 3]. Progression from this basic linear pattern to functional devices required a gradual design evolution. Simple lines provided core insights into isolated LIG, while rectangles simulated conductive areas linked through line intersections. This stepwise increase in complexity facilitated the shift from individual elements to complex geometries. Further, it supported stepwise assessment of prediction accuracy, evolving from basic forms to elaborated devices, common in flexible electronics.

The strategy had to demonstrate whether simplistic line-based training data effectively guide the optimization of complex shapes, accelerating data acquisition and automated design improvements without requiring shape-specific datasets and characteristics. Rectangular patterns formed from overlapping parallel lines [36], with a schematic depicted in Figure 7c. These line intersections resulted from defocus-induced beam expansion, as illustrated in Figure 1d. Overlapped areas thus received double exposure, leading to a more complex substrate graphitization that our straightforward model had to address. To showcase practical application, we designed a flexible circuit (demonstrator) that integrated LIG electrodes as current-limiting linear resistors, coupling a light-emitting diode (LED) with a power source. The electronic schematic appears in Figure 7d, and the targeted LIG properties derived from Equations (S1)–(S3) in Note S2.

4.3 | Materials and Equipment

PI film (Kapton 300HN, DuPont, 75 μm thick) served as a substrate for LIG formation. Borosilicate glass plates (Borofloat 33, Schott AG, 2 mm thick, 100 × 100 mm^2) were used as support and confinement. The fiber-laser system (PIRANHA, ACSYS Lasertechnik GmbH, 1064 nm wavelength, maximum power 20 W, frequency 20 kHz, pulse duration 2 μm, unidirectional patterning mode) was employed for sample manufacturing. A commercially available conductive varnish (47% silver, VS Electronic Vertrieb GmbH) was applied on validation rectangles and for demonstrator manufacturing. An orange-colored LED (model APDA3020LSECK/J4-PF, Kingbright Electronic Europe GmbH, V_{LED} = 1.8 V, I_{LED} = 2 mA) was applied for the demonstrator. A standard 5VDC USB-A port was used as a power source.

Optical microscopy and measurements were conducted using the Keyence VHX-7000 digital microscope. Electrical measurements were performed via the LCR-meter BK891 (B&K Precision Corp.), and a manual probe station Cascade MPS150 (FormFactor Inc.) equipped with two positioner kits DPP210. Training, validation, and testing were conducted on a system equipped with 256 GB of RAM, a 32-core processor Ryzen Threadripper 3970x (64 logical cores), and an NVIDIA TITAN RTX GPU with 24 GB VRAM (driver version 537.42, CUDA 11.8), running 64-bit Microsoft Windows 11 Enterprise (version 22H2). Eight CUDA workers were used during training, with one worker allocated for validation and testing. Implementation was performed in Python 3.12.8 with PyTorch 2.5.0.

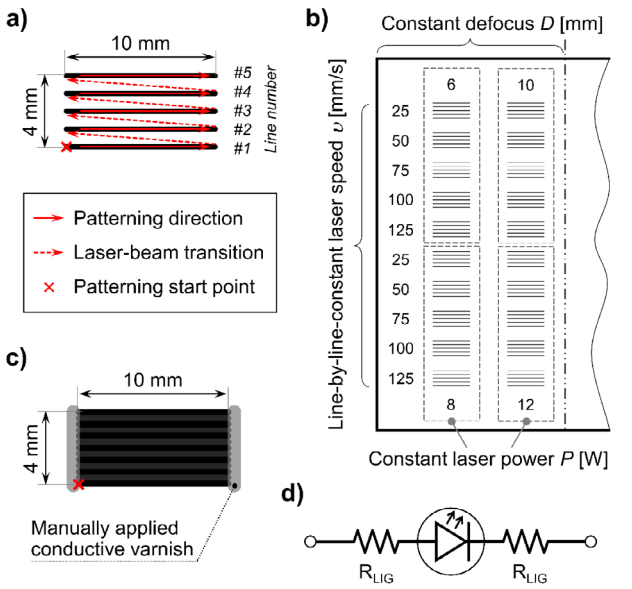

FIGURE 7 | Designs of physical samples and a functional demonstrator illustrating the progression from basic laser-induced graphene (LIG) patterns to complex devices on polyimide substrates. (a) Digital layout of a lineset consisting of five parallel single lines and the corresponding laser-patterning procedure. (b) Matrix arrangement of linesets on a substrate, grouped according to identical laser beam parameters. (c) Schematic of the validation rectangle formed by a single digital lineset, including the locations where conductive silver-based varnish is subsequently applied to connect individual lines. (d) Electronic schematic of the demonstrator circuit, in which machine learning predicts and controls the fabrication parameters of two identical LIG electrodes to achieve predesigned current-limiting resistances R_{LIG}.

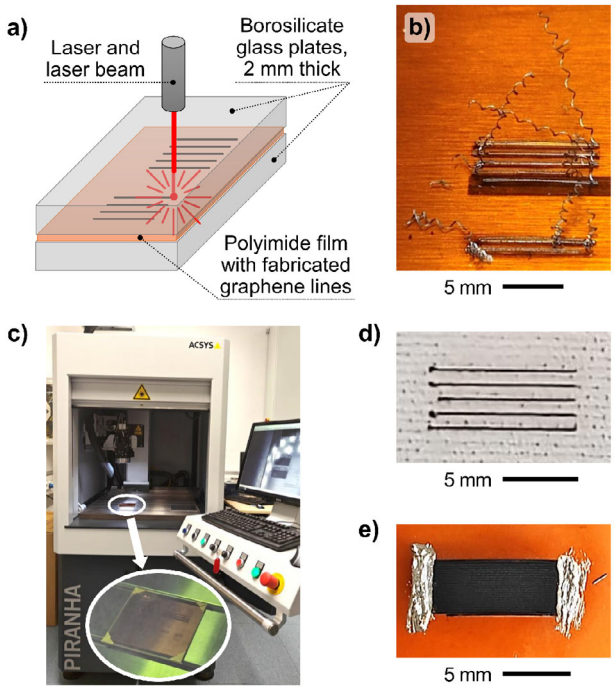

FIGURE 8 | Fabrication of laser-induced graphene (LIG) samples on polyimide substrates. (a) Schematic of the laser-patterning process and the substrate assembly confined between two glass plates. (b) Example of bulky LIG delamination occurring in an open-air configuration, showing helical structures. (c) The ACSYS PIRANHA fiber-laser system used in this work. Inset: substrate assembly (100 × 100 mm^2) positioned on the equipment table during laser patterning, with the laser beam visible in the top-left area. (d) Example of non-bulky LIG delamination after manual removal of a glass plate, where detached lines adhere to the glass plate placed on bonded fabric. (e) Validation rectangle sample with conductive varnish manually applied to the line ends for electrical connection.

4.4 | Fabrication and Characterization Procedures

LIG samples were produced on PI substrates confined between two borosilicate glass plates. Such standardized assembly, illustrated schematically in Figure 8a, prevented substrate warping, ensured uniform laser exposure and consistent defocus, minimized thermal deformation, and protected the equipment bed from stray radiation. This confinement approach avoided bulky LIG delamination—visible in Figure 8b and typical of open-air configurations—improved fabrication consistency, and enhanced graphitization density [1, 3]. Borosilicate glass absorbs approx. 5% to 10% of the laser energy at 1064 nm and causes minor diffraction. However, these effects remained uniform across samples due to consistent procedures, with associated variance incorporated into the unfiltered training data. Laser patterning involved varying power P (0.5–20 W), scanning speed υ (50–500 mm/s), and defocus D (−5 to +5 mm) to modulate energy density U. This setup enabled fabrication of single lines and rectangular patterns with targeted LIG properties. The fiber-laser system and glass confinement are shown in Figure 8c.

After lasing, glass plates were removed manually without measures to prevent non-bulky LIG detachment, as demonstrated in Figure 8d. Such partial delamination, better visible in Figure S2, S3b–c, and S4c,d, reflected real-world conditions and enhanced model robustness, as it increased resistance variance, but was retained in the data. Then, samples were transferred or characterized in situ. For lines, width W was measured by optical microscopy, encompassing both the LIG core and surrounding transitional zones. Linear electrical resistance R was determined with a probe station. Both attributes involved 5 to 15 points per line, which were subsequently averaged. For rectangular samples, direct measurement of individual line resistance and width proved impractical due to line overlaps. Therefore, line ends received conductive varnish to connect all lines uniformly, as in Figure 8e, and rectangles were considered as a set of parallel resistors.

4.5 | Data Collection and Evaluation

During sample characterization, measured properties of LIG samples were linked to the corresponding lasing parameters. The applied laser energy density U was derived from these LBP using Equations 1–4. This step provided a standardized metric that facilitated consistent evaluation of properties across various energy levels [44]:

$$U = \frac{P}{\upsilon \cdot A_F} \cdot \frac{1}{\Delta A_F(D)}, \left[\frac{J}{mm^3}\right] \quad (1)$$

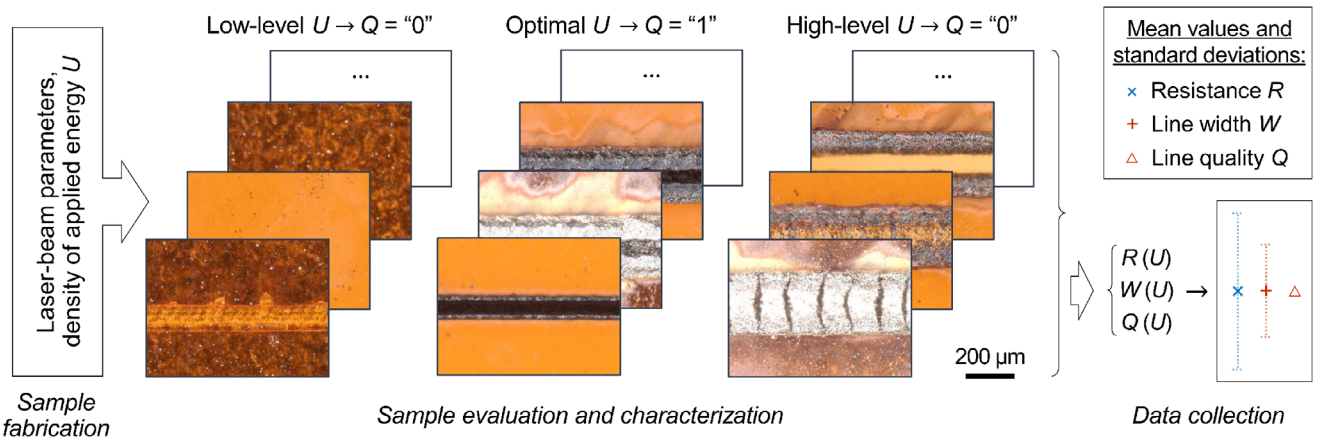

FIGURE 9 | Schematic of the data-collection workflow for laser-induced graphene samples. For each fabricated sample, the applied energy density U is computed from the corresponding laser beam parameters. Following manual evaluation and characterization, the collected data are grouped by U values, with mean values and standard deviations calculated for each group. These interrelated data points are then compiled into datasets suitable for subsequent analysis and application. Standard deviations are assessed for most properties but are of limited applicability to the binary quality indicator Q.

where A_F is the laser-beam cross-sectional area in the laser-focus point F:

$$A_F = \frac{\pi}{4} \cdot d_F^2, \ [mm^2] \tag{2}$$

and $\Delta A_F(D)$ is the defocus-induced increase of A_F near F:

$$\Delta A_F \ (D) = \frac{\pi}{4} \cdot c_D^2, \ [mm^2] \tag{3}$$

with $d_F = 50$ µm is the nominal laser-beam diameter in F, and c_D is an empirical coefficient of the d_F increase near F, with respect to D:

$$c_D = 1 + 0.1 \cdot |D| \ , \ [1] \ , \ |D| \lessapprox 0.7 \ mm \tag{4}$$

Conductivity-specific quality Q served as a binary indicator: it was set to "1" for LIG lines that successfully formed and exhibited conductivity, and "0" for those that did not form, were burned, or were otherwise damaged. Any line showing a resistance $R \geq 5$ kΩ/mm qualified as non-conductive.

For validation rectangles, the equivalent resistance R_{eq} for the parallel resistor configuration was computed via Equation 5, based on dimensions L = 10 mm and H = 4 mm, as depicted in Figure 3c:

$$R_{eq} = \frac{R \cdot W \cdot L}{H \cdot \sqrt{2}} \ [\Omega] \tag{5}$$

The overall data collection workflow, shown in Figure 9, proceeded as follows. For each fabricated sample, U was first calculated from its LBP. Samples then underwent manual evaluation and characterization. Collected data were grouped according to U values, with mean values and standard deviations determined for each group. These interrelated data points were compiled into cohesive datasets ready for further analysis. Standard deviations applied to most properties, although they held limited relevance for the binary nature of Q.

4.6 | Metrics

To address the challenge of comparing results across studies (stemming from the wide variety of metrics reported in the literature), a comprehensive set of evaluation metrics was employed in this work.

The variance of the training data was estimated using an unbiased relative standard deviation (*%RSD**), as defined in Equation 6 [33]. *%RSD** scores exceeding the critical threshold $\%RSD^*_{crit} = 0.33$ signify high variance, and typically necessitates data-improvement techniques, such as filtering [34, 35]. However, no such operations were applied in the present study:

$$\%RSD^* = \left(1 + \frac{1}{4n}\right) \cdot \frac{s}{\bar{x}}, \ [1] \tag{6}$$

where n, s, and $\bar{x}$ represent the number of samples, the standard deviation, and the arithmetic mean, respectively.

Prediction accuracy (acc_P) served as the primary metric. For each evaluated variable X, it was calculated in the range [0, 1] as the min-to-max normalized ratio between its NN-predicted values (X_{NN}) and the reference values (X_{Ref}), according to Equation 7 [44]:

$$acc_P \ (X) = \frac{\min\left(X_{NN}, \ X_{Ref}\right)}{\max\left(X_{NN}, \ X_{Ref}\right)} \ , \ [1] \tag{7}$$

Analogously, trend correlation (acc_T) quantified the alignment of X_{Ref} values with statistically expected values (X_T), based on the distribution trend of X_{Ref}, as given in Equation 8. This metric allowed assessment of changes in data variance as a function of U. Values of acc_T also ranged from 0 to 1, with 1 denoting perfect agreement between the actual and expected values:

$$acc_T \ (X) = \frac{\min\left(X_{Ref}, \ X_T\right)}{\max\left(X_{Ref}, \ X_T\right)} \ , \ [1] \tag{8}$$

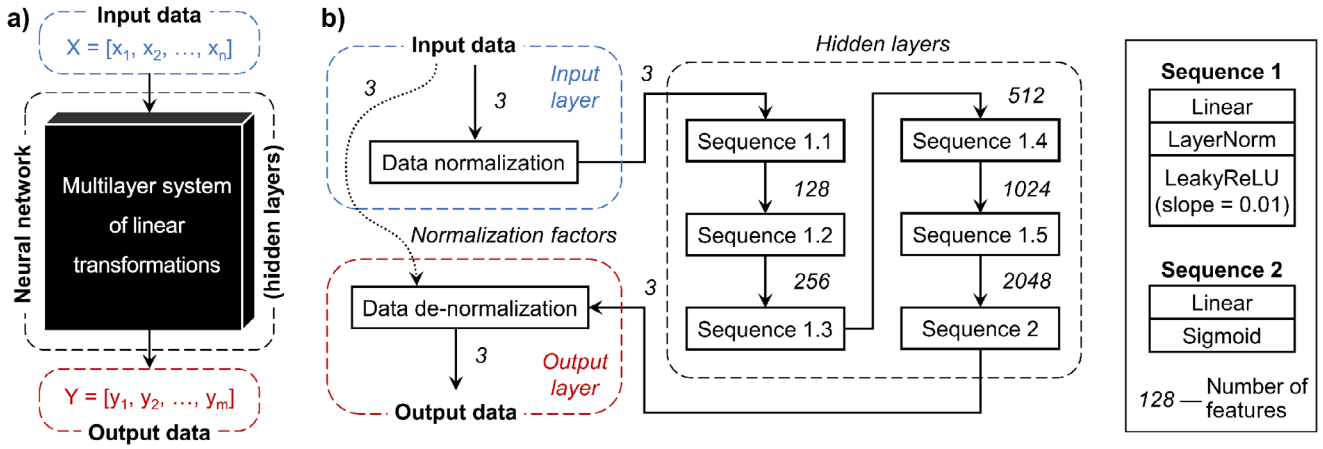

FIGURE 10 | Architecture and operation of the neural network used for bidirectional prediction in laser-induced graphene fabrication. (a) Operating principle, in which a plain neural network functions as a set of interconnected linear transformations linking input and output variables to form a numerical blackbox prediction model. The number of variables (features) is defined by the model architecture, while the coefficients of the linear equations remain not human-interpretable. (b) Workflow schematic showing min-max normalization of input data, followed by six stepwise transformations in the sequences of hidden layers. The resulting values are de-normalized using additionally transmitted normalization factors to produce the output data.

For the twofold control, restoration accuracy (acc_R) was determined by directly comparing the original input (X_{in}) with the restored output (X_{out}):

$$acc_R\ (X) = \frac{\min\left(X_{in},\ X_{out}\right)}{\max\left(X_{in},\ X_{out}\right)},\ [1] \tag{9}$$

To evaluate the central tendency of the NN prediction for lasing parameters LBP or LIG properties PP, the corresponding accuracies—acc_P, acc_T, or acc_R, treated as normalized results—were combined using the geometric mean [45]. This yielded a joint accuracy J that integrated the accuracies of interrelated variables $acc(X)$:

$$J = \begin{bmatrix} \sqrt[3\cdot k]{acc\,(P)\cdot acc\,(\upsilon)\cdot acc\,(D)}, & LBP\ :\ all\ datasets \\ \sqrt[3\cdot k]{acc\,(R)\cdot acc\,(W)\cdot acc\,(Q)}, & PP\ :\ datasets\ A, B, D, E \\ \sqrt[2\cdot k]{acc\left(R_{eq}\right)\cdot acc\,(Q)}, & PP\ :\ dataset\ C \end{bmatrix},\ [1] \tag{10}$$

where k denotes the number of sequential NNs involved. Here, $k = 1$ for the direct and inverse prediction workflows, and $k = 2$ for the twofold control.

Linear regression analysis [46] was performed on datasets A–E to examine the relationship between input and output variables, and to demonstrate its inferior predictive performance relative to the proposed approach. Additionally, the coefficient of determination (R^2) assessed model fit to the ground-truth data, while the Pearson correlation coefficient (PCC) measured the linear association between actual and predicted values. Both metrics were interpreted using the Chaddock scale, with thresholds defined as follows: >0.9 (very strong), 0.7–0.9 (strong, indicating reliable predictions), 0.5–0.7 (moderate), 0.2–0.5 (weak), and <0.2 (negligible) [47, 48].

4.7 | Neural Network

The developed NN facilitated direct numerical mapping from input to output variables, as depicted in Figure 10a. Lasing parameters (LBP: laser power P [W], speed υ [mm/s], and defocus D [mm]) and LIG properties (PP: linear electrical resistance R [Ω/mm], dimensional width W [μm], and conductivity-specific line quality Q [1]) were interchangeably used as inputs and outputs depending on the prediction direction. The NN formed a blackbox prediction model comprising a series of linear transformations (i.e., equations). The number and dimensionality of these transformations were determined by the NN architecture. During training, the coefficients of the related linear equations were automatically computed and optimized to maximize predictive performance. The architecture and operational workflow of the NN are illustrated schematically in Figure 10b.

The architecture consisted of input (blue-dashed frame) and output (red-dashed frame) layers for the respective datasets, along with six hidden layers (MLP, black-dashed frame). These hidden layers formed the core blackbox component. Six linear layers functioned as feature-transforming equations, interconnected by LayerNorm normalization and LeakyReLU activation function (negative slope of 0.01) for data transfer [44]. Sequences 1.1 through 1.5 were identical, except for the number of features in their linear layers. In the final Sequence 2, a Sigmoid activation function constrained the output to range [0, 1], acting as a smooth and differentiable filter.

To prevent sigmoid saturation, linear layers were initialized with weights uniformly sampled from $[(-1)/\sqrt{y};\ 1/\sqrt{y}]$, where y denotes the number of input features; and biases were set to 0.01. Batch normalization of intermediate results further contributed to stability. Normalization factors, computed individually for each variable before training, were concatenated to the input data to facilitate accurate de-normalization in the output layer.

Thus, a faithful reconstruction of the original variable ranges was ensured.

Input data were min-max normalized to the range [0, 1] before processing in the hidden layers. Then, the feature dimensionality increased progressively from three to 128, doubled stepwise to 2048, and then reduced back to three. After final de-normalization, the NN emitted predicted values for the target variables: PP or LBP, depending on the prediction direction.

Training employed the mean absolute error (L1 loss) scaled by an empirical factor $\lambda = 10^3$, combined with the AdaM optimizer and a sinusoidal gradient descent [49–51]. The learning rate decreased gradually from 2×10^{-5} to 1×10^{-5} over 125 epochs. After each epoch, validation was performed on 10 randomly selected training samples. The training dataset (Dataset A) was randomly divided into 90% training and 10% validation subsets. Upon training, the NN was evaluated on independent validation datasets (Datasets B and C).

Acknowledgements

This work was funded by the program Material Systems Engineering of the Helmholtz Association. Open access funding was enabled and organized by Project DEAL. Gerardo Hernández-Sosa thanks the Deutsche Forschungsgemeinschaft (DFG, German Research Foundation) for the financial support (Heisenbergprofessur, HE 7056/7-1).

Open access funding enabled and organized by Projekt DEAL.

Conflicts of Interest

None of the authors have a conflict of interest to disclose.

Data Availability Statement

The datasets generated and/or analyzed during the current study are available in the KITopen repository, https://doi.org/10.35097/rr0ja48j7cqjud5b.

References

1. M. Abdulhafez, G. N. Tomaraei, and M. Bedewy, "Fluence-Dependent Morphological Transitions in Laser-Induced Graphene Electrodes on Polyimide Substrates for Flexible Devices," *ACS Applied Nano Materials* 4 (2021): 2973–2986, https://doi.org/10.1021/acsanm.1c00101.

2. K. Avinash and F. Patolsky, "Laser-Induced Graphene Structures: From Synthesis and Applications to Future Prospects," *Materials Today* 70 (2023): 104–136, https://doi.org/10.1016/j.mattod.2023.10.009.

3. S. Bai, Y. Tang, L. Lin, et al., "Investigation of Micro/Nano Formation Mechanism of Porous Graphene Induced by CO_2 Laser Processing on Polyimide Film," *Journal of Manufacturing Processes* 84 (2022): 555–564, https://doi.org/10.1016/j.jmapro.2022.10.037.

4. G. Ghimire, F. Noormohammadi, J. Kohl, H. Devenport, and P. A. Johnson, "Machine Learning Optimization of Laser-Induced Graphene Parameters for Surface-Enhanced Raman Spectroscopic Detection of Glucose," *Sensors and Actuators B: Chemical* 432 (2025): 137466, https://doi.org/10.1016/j.snb.2025.137466.

5. R. Ye, D. K. James, and J. M. Tour, "Laser-Induced Graphene: From Discovery to Translation," *Advanced Materials* 31 (2019): 1803621, https://doi.org/10.1002/adma.201803621.

6. Z. Zhang, H. Zhu, W. Zhang, et al., "A Review of Laser-Induced Graphene: From Experimental and Theoretical Fabrication Processes to Emerging Applications," *Carbon* 214 (2023): 118356, https://doi.org/10.1016/j.carbon.2023.118356.

7. H. Wahab, V. Jain, A. S. Tyrrell, M. A. Seas, L. Kotthoff, and P. A. Johnson, "Machine-Learning-Assisted Fabrication: Bayesian Optimization of Laser-Induced Graphene Patterning Using In-Situ Raman Analysis," *Carbon* 167 (2020): 609–619, https://doi.org/10.1016/j.carbon.2020.05.087.

8. H.-S. Park, B. R. Maddox, E. Giraldez, et al., "High-Resolution 17–75 keV Backlighters for High Energy Density Experiments," *Physics of Plasmas* 15 (2008): 072705, https://doi.org/10.1063/1.2957918.

9. R. G. Zonov, K. G. Mikheev, A. A. Chulkina, I. A. Zlobin, and G. M. Mikheev, "Effect of Laser Power on the Structure and Specific Surface Area of Laser-Induced Graphene," *Diamond and Related Materials* 148 (2024): 111409, https://doi.org/10.1016/j.diamond.2024.111409.

10. N.-K. Yang, Y.-K. Shin, S. Park, et al., "Exploring Graphene Structure, Material Properties, and Electrochemical Characteristics Through Laser-Induced Temperature Analysis," *Micro and Nano Systems Letters* 12 (2024): 8, https://doi.org/10.1186/s40486-024-00198-x.

11. B. Xie, Y. Guo, Y. Chen, et al., "Dual-Indicators Machine Learning Assisted Processing High-Quality Laser-Induced Fluorine-Doped Graphene and Its Application on Droplet Velocity Monitoring Sensor," *Carbon* 226 (2024): 119231, https://doi.org/10.1016/j.carbon.2024.119231.

12. H. Le, A. Minhas-Khan, S. Nambi, G. Grau, W. Shen, and D. Wu, "Predicting the Sheet Resistance of Laser-Induced Graphitic Carbon Using Machine Learning," *Flexible and Printed Electronics* 8 (2023): 035013, https://doi.org/10.1088/2058-8585/acedbf.

13. J. C. Santos-Ceballos, F. Salehnia, A. Romero, and X. Vilanova, "Application of Digital Twins for Simulation Based Tailoring of Laser Induced Graphene," *Scientific Reports* 14 (2024): 10363, https://doi.org/10.1038/s41598-024-61237-6.

14. M.-C. Popescu, V. E. Balas, L. Perescu-Popescu, and N. Mastorakis, "Multilayer Perceptron and Neural Networks," *WSEAS Transactions on Circuits and Systems* 8 (2009): 579–588, https://doi.org/10.5555/1639537.1639542.

15. V. Buhrmester, D. Münch, and M. Arens, "Analysis of Explainers of Black Box Deep Neural Networks for Computer Vision: A Survey," *Machine Learning and Knowledge Extraction* 3 (2021): 966–989, https://doi.org/10.3390/make3040048.

16. J. E. Dobson, "On Reading and Interpreting Black Box Deep Neural Networks," *International Journal of Digital Humanities* 5 (2023): 431–449, https://doi.org/10.1007/s42803-023-00075-w.

17. S. Ali, T. Abuhmed, S. El-Sappagh, et al., "Explainable Artificial Intelligence (XAI): What We Know and What Is Left to Attain Trustworthy Artificial Intelligence," *Information Fusion* 99 (2023): 101805, https://doi.org/10.1016/j.inffus.2023.101805.

18. A. T. Hui, S. S. Ahn, C. T. Lye, and J. Deng, "Ethical Challenges of Artificial Intelligence in Health Care: A Narrative Review," *Ethics in Biology, Engineering and Medicine: An International Journal* 12 (2021): 55–71, https://doi.org/10.1615/EthicsBiologyEngMed.2022041580.

19. C. Luo, A.-J. Li, J. Xiao, M. Li, and Y. Li, "Explainable and Generalizable AI-Driven Multiscale Informatics for Dynamic System Modelling," *Scientific Reports* 14 (2024): 18219, https://doi.org/10.1038/s41598-024-67259-4.

20. Z. Yang, D. Eddy, S. Krishnamurty, et al., *Investigating Grey-box Modeling for Predictive Analytics in Smart Manufacturing*, American Society of Mechanical Engineers Digital Collection, 2017, DETC2017–67794, https://doi.org/10.1115/DETC2017-67794.

21. S. Estrada-Flores, I. Merts, B. De Ketelaere, and J. Lammertyn, "Development and Validation of "Grey-Box" Models for Refrigeration Applications: A Review of Key Concepts," *International Journal of Refrigeration* 29 (2006): 931–946, https://doi.org/10.1016/j.ijrefrig.2006.03.018.

22. M. Hosseini, A. Shahri, K. Phalp, and R. Ali, "Engineering Transparency Requirements: A Modelling and Analysis Framework," *Information Systems* 74 (2018): 3–22, https://doi.org/10.1016/j.is.2017.12.008.

23. M. Xia, H. Shao, Z. Huang, Z. Zhao, F. Jiang, and Y. Hu, "Intelligent Process Monitoring of Laser-induced Graphene Production With Deep Transfer Learning," *IEEE Transactions on Instrumentation and Measurement* 71 (2022): 1–9, https://doi.org/10.1109/TIM.2022.3186688.

24. K. Sattari, L. Eddy, J. L. Beckham, et al., "A Scientific Machine Learning Framework to Understand Flash Graphene Synthesis," *Digital Discovery* 2 (2023): 1209–1218, https://doi.org/10.1039/D3DD00055A.

25. X. Chen, K. W. Gan, S. H. Pu, M. Jalalvand, and A. R. Hamilton, "Laser-Induced Graphene as an Embedded Sensor for Impact Damage in Composite Structures Assisted by Machine Learning," *Structural Health Monitoring* 25 (2025): 1–17, https://doi.org/10.1177/14759217241311516.

26. R. Murray, M. Burke, D. Iacopino, and A. J. Quinn, "Design of Experiments and Optimization of Laser-Induced Graphene," *ACS Omega* 6 (2021): 16736–16743, https://doi.org/10.1021/acsomega.1c00309.

27. J. L. Beckham, K. M. Wyss, Y. Xie, et al., "Machine Learning Guided Synthesis of Flash Graphene," *Advanced Materials* 34 (2022): 2106506, https://doi.org/10.1002/adma.202106506.

28. W. Jin, J. Pei, P. Xie, J. Chen, and H. Zhao, "Machine Learning-Based Prediction of Mechanical Properties and Performance of Nickel–Graphene Nanocomposites Using Molecular Dynamics Simulation Data," *ACS Applied Nano Materials* 6 (2023): 12190–12199, https://doi.org/10.1021/acsanm.3c01919.

29. S. Kim, M. Cho, and S. Jung, "The Design of an Inkjet Drive Waveform Using Machine Learning," *Scientific Reports* 12 (2022): 4841, https://doi.org/10.1038/s41598-022-08784-y.

30. J. Huang, L. J. Segura, T. Wang, G. Zhao, H. Sun, and C. Zhou, "Unsupervised Learning for the Droplet Evolution Prediction and Process Dynamics Understanding in Inkjet Printing," *Additive Manufacturing* 35 (2020): 101197, https://doi.org/10.1016/j.addma.2020.101197.

31. M. Zhao, H. Wei, Y. Mao, C. Zhang, T. Liu, and W. Liao, "Predictions of Additive Manufacturing Process Parameters and Molten Pool Dimensions With a Physics-informed Deep Learning Model," *Engineering* 23 (2023): 181–195, https://doi.org/10.1016/j.eng.2022.09.015.

32. M. Polomoshnov, N. M. Nair, G. Hernandez-Sosa, and M. Reischl, *Datasets to the Bidirectional Process Prediction in the Laser-Induced-Graphene Production Using Blackbox Deep Learning*, KITOpen, (2025), https://doi.org/10.35097/rr0ja48j7cqjud5b.

33. R. R. Sokal and F. J. Rohlf, *Biometry: The Principles and Practice of Statistics in Biological Research*, 4th ed., W. H. Freeman and Company, (2012), 58.

34. M. G. Vangel, "Confidence Intervals for a Normal Coefficient of Variation," *The American Statistician* 50 (1996): 21–26, https://doi.org/10.2307/2685039.

35. J. Forkman and S. Verrill, "The Distribution of McKay's Approximation for the Coefficient of Variation," *Statistics & Probability Letters* 78 (2008): 10–14, https://doi.org/10.1016/j.spl.2007.04.018.

36. Y. Steksova, A. C. Bressi, M. Galliani, et al., "Laser-Induced Graphene From Waste Almond Shells," *Advanced Functional Materials* (2025): 07462, https://doi.org/10.1002/adfm.202507462.

37. J. Lin, Z. Peng, Y. Liu, et al., "Laser-Induced Porous Graphene Films From Commercial Polymers," *Nature Communications* 5 (2014): 5714, https://doi.org/10.1038/ncomms6714.

38. W. Ma, J. Zhu, Z. Wang, W. Song, and G. Cao, "Recent Advances in Preparation and Application of Laser-Induced Graphene in Energy Storage Devices," *Materials Today Energy* 18 (2020): 100569, https://doi.org/10.1016/j.mtener.2020.100569.

39. K. G. Mikheev, R. G. Zonov, N. V. Chuchkalov, and G. M. Mikheev, "The Electrical Resistance of Laser-Induced Graphene Synthesized by a Continuous-Wave CO_2-Laser," *Physics of the Solid State* 66 (2024), https://doi.org/10.61011/PSS.2024.02.57924.5.

40. B. Plank, "The "Problem" of Human Label Variation: On Ground Truth in Data, Modeling and Evaluation," in Proceedings of the 2022 Conference on Empirical Methods in Natural Language Processing, eds. Y. Goldberg, Z. Kozareva, Y. Zhang, Association for Computational Linguistics, (2022): 10671–10682, https://doi.org/10.18653/v1/2022.emnlp-main.731.

41. J.-Y. Zhu, T. Park, P. Isola, and A. A. Efros, "Unpaired Image-to-Image Translation Using Cycle-Consistent Adversarial Networks," in 2017 IEEE International Conference on Computer Vision (ICCV), (IEEE, 2017): 2242–2251, https://doi.org/10.1109/ICCV.2017.244.

42. M. Böhland, R. Bruch, S. Bäuerle, L. Rettenberger, and M. Reischl, "Improving Generative Adversarial Networks for Patch-Based Unpaired Image-to-Image Translation," *IEEE Access* 11 (2023): 127895, https://doi.org/10.1109/ACCESS.2023.3331819.

43. R. Bruch, F. Keller, M. Böhland, et al., "Synthesis of Large Scale 3D Microscopic Images of 3D Cell Cultures for Training and Benchmarking," *PLoS ONE* 18 (2023): 0283828, https://doi.org/10.1371/journal.pone.0283828.

44. M. Polomoshnov, K.-M. Reichert, L. Rettenberger, et al., "Image-Based Identification of Optical Quality and Functional Properties in Inkjet-Printed Electronics Using Machine Learning," *Journal of Intelligent Manufacturing* 36 (2025): 2709–2726, https://doi.org/10.1007/s10845-024-02385-4.

45. P. J. Fleming and J. J. Wallace, "How Not to Lie With Statistics: The Correct Way to Summarize Benchmark Results," *Communications of the ACM* 29 (1986): 218–221, https://doi.org/10.1145/5666.5673.

46. D. L. Mohr, *Statistical Methods*, (Academic Press, 2010): 325–327.

47. R. Borovskaya, D. Krivoguz, S. Chernyi, E. Kozhurin, V. Khorosheltseva, and E. Zinchenko, "Surface Water Salinity Evaluation and Identification for Using Remote Sensing Data and Machine Learning Approach," *Journal of Marine Science and Engineering* 10 (2022): 257, https://doi.org/10.3390/jmse10020257.

48. R. B. D. Saura and R. J. M. Andante, "Detection of Cyanide in Freshwater Fishes Relative to Sex Dimorphism Using Landmark-Based Geometric Morphometrics," *International Journal of Biosciences* 12 (2018): 176–192, https://doi.org/10.12692/ijb/12.2.176-192.

49. I. Loshchilov and F. Hutter, "SGDR: Stochastic Gradient Descent With Warm Restarts," in 5th International Conference on Learning Representations (ICLR), OpenReview.net, 2017, https://doi.org/10.48550/arXiv.1608.03983.

50. R. M. Schmidt, F. Schneider, and P. Hennig, "Descending Through a Crowded Valley: Benchmarking Deep Learning Optimizers," in Proceedings of the 38th International Conference on Machine Learning, (PMLR, 2021): 9367–9376, https://doi.org/10.48550/arXiv.2007.01547.

51. P. T. Sivaprasad, F. Mai, T. Vogels, M. Jaggi, and F. Fleuret, "Optimizer Benchmarking Needs to Account for Hyperparameter Tuning," in Proceedings of the 37th International Conference on Machine Learning, (PMLR, 2020): 9036–9045, https://doi.org/10.48550/arXiv.1910.11758.

Supporting Information

Additional supporting information can be found online in the Supporting Information section.

Supporting File: admt71016-sup-0001-SuppMat.pdf.